WILEY
Aggregate
Open Access

RESEARCH ARTICLE OPEN ACCESS

3D Rotary Wet-Spinning (RoWS) Biofabrication Directly Affects Proteomic Signature and Myogenic Maturation in Muscle Pericyte–Derived Human Myo-Substitute

Alessio Reggio[1] | Claudia Fuoco[2] | Francesca De Paolis[2,3] | Rebecca Deodati[2,3] | Stefano Testa[4] | Nehar Celikkin[5] | Marina Volpi[6] | Sergio Bernardini[2] | Ersilia Fornetti[2] | Jacopo Baldi[7] | Roberto Biagini[7] | Dror Seliktar[8] | Carmine Cirillo[9] | Wojciech Swieszkowski[6] | Paolo Grumati[9,10] | Stefano Cannata[2] | Marco Costantini[5] | Cesare Gargioli[2]

[1]Saint Camillus International, University of Health Sciences, Rome, Italy | [2]Department of Biology, University of Rome Tor Vergata, Rome, Italy | [3]PhD Program in Cellular and Molecular Biology, Department of Biology, University of Rome, "Tor Vergata", Rome, Italy | [4]Aix-Marseille University, INSERM, MMG, Marseille Medical Genetics, Marseille, France | [5]Institute of Physical Chemistry, Polish Academy of Sciences, Warsaw, Poland | [6]Faculty of Materials Science and Engineering, Warsaw University of Technology, Warsaw, Poland | [7]IRCCS Regina Elena National Cancer Institute, Rome, Italy | [8]Faculty of Biomedical Engineering, Technion Israel Institute of Technology, Haifa, Israel | [9]Telethon Institute of Genetics and Medicine (TIGEM), Pozzuoli, Italy | [10]Department of Clinical Medicine and Surgery, Federico II University, Naples, Italy

Correspondence: Marco Costantini (mcostantini@ichf.edu.pl) | Cesare Gargioli (cesare.gargioli@uniroma2.it)

Received: 19 September 2024 | **Revised:** 3 December 2024 | **Accepted:** 5 December 2024

Funding: This work was supported by AFM-Téléthon (23551), Fondazione Telethon (TMPGMFU22TT), Muscular Dystrophy Association (MDA 968551), National Science Centre Poland (NCN) within SONATA BIS 12 (project no. 2022/46/E/ST8/00284), and Ministero dell'Istruzione, dell'Università e della Ricerca (PRIN funding scheme no. 201742SBXA_004 and 2022F37JRF).

Keywords: 3D printing | proteomic | skeletal muscle | tissue engineering

ABSTRACT

Skeletal muscle tissue engineering (SMTE) has recently emerged to address major clinical challenges such as volumetric muscle loss (VML). Here, we report a rotary wet-spinning (RoWS) biofabrication technique for producing human myo-substitutes with biomimetic architectures and functions. Here, we demonstrate how the proposed technique may be used to establish a well-tailored, anisotropic microenvironment that promotes myogenic differentiation of human skeletal muscle–derived pericytes (hPeri). Using high-resolution mass spectrometry–based proteomics with the integration of literature-derived signaling networks, we uncovered that (i) a 3D biomimetic matrix environment (PEG-fibrinogen) confers a less mitogenic microenvironment compared to standard 2D cultures, favoring the formation of contractile-competent bundles of pericyte-derived myotubes in an anchoring-independent 3D state and (ii) the RoWS method promotes an upregulation of muscle matrix structural protein besides increasing contractile machinery proteins with respect to 3D bulk cultures. Finally, in vivo investigations demonstrate that the 3D-biofabricated myo-substitute is fully compatible with the host ablated muscular tissue, exhibiting myo-substitute engraftment and muscle regeneration in a mouse model of VML. Overall, the results show that RoWS offers a superior capability for controlling the myogenic differentiation process on a macroscale and, with future refining, may have the potential to be translated into clinical practice.

Alessio Reggio and Claudia Fuoco contributed equally to this work.

1 | Introduction

Over the last decade, biofabrication technologies have brought a new wave of enthusiasm in the tissue engineering community as a potential option for the fabrication of architecturally complex and functionally biomimetic tissue/organ substitutes. The increasing interest in such systems is justified by their unprecedented advantages that enable building multimaterial, cellularized constructs with high spatial resolution, repeatability, and three-dimensional (3D) biomimetic structural complexity. In the context of skeletal muscle tissue engineering (SMTE), biofabrication technologies have demonstrated great potential in guiding the alignment and differentiation of myogenic precursors—including human primary cells—both in in vitro and in vivo models [1–4]. Notable examples in the field include the assembly of multicellular models for the in vitro recapitulation of the neuromuscular junction (NMJ) or myotendinous junction (MTJ) complexity, mimicking exercise and pharmacological response, or the fabrication of artificial skeletal muscles (SM) for regenerative medicine applications in small animal models [5–8]. Moreover, biofabrication strategies have been proposed for the manufacturing—though to a small scale (approx. 1 cm^3)—of whole cut, bovine meat-like tissue containing muscle, fat, and vasculature tissue [9, 10].

Despite such promising and encouraging results, many fundamental biological aspects remain to be elucidated. It has not been thoroughly investigated how the biofabricated microenvironment rewires muscle progenitors to form functional muscle bundles. Moreover, it is not clear whether there is a difference in terms of myogenic process modulation between biofabricated muscles and engineered muscle constructs obtained using conventional approaches (e.g., two-dimensional (2D) or 3D bulk hydrogels). Such missing information is of the utmost importance, as it may help to unravel the complexity of neo-muscle tissue formation and to develop improved strategies for its assembly in vitro. Herein, a biofabrication strategy—namely 3D rotary wet-spinning (RoWS)—comprising a microfluidic printing head was employed to fabricate biomimetic, aligned core–shell hydrogel constructs where human skeletal muscle-derived pericytes (hPeri) were encapsulated. Being a peculiarly designed strategy for engineering SM constructs, RoWS is a significantly efficient method for producing volumetric muscle constructs compared to extrusion-based biofabrication as the fiber production speed is approximately 4.2 m/min. Moreover, the specific design of the microfluidic printing head in RoWS enables the extrusion of a high number of cells embedded in low-viscosity hydrogel precursor in a confined volume without exposing the cells to high shear stresses. The 3D RoWS biofabrication platform and the materials used here are particularly designed for creating physically and biologically relevant confined anisotropic architecture to induce myotube formation. As reported in previous studies, SM-derived hPeri are a powerful source of competent myogenic precursor cells, and such myogenic potential is favored by culturing these cells in 3D hydrogel matrices [11]. Hence, for this study, hPeri have been chosen as myogenic progenitors because they show a robust differentiation capability into muscle besides angiogenic activity promoting blood vessel recruitment, fundamental to support implant survival and integration into host tissue [11–14]. Moreover, to induce myogenic differentiation in biofabricated structures, we require a cell density of 2×10^7 cells/mL. Pericytes enable to reach this target efficiently, in a relatively short time frame, without compromising myogenic properties [15, 16]. The myogenic capacity of the biofabricated hPeri-loaded samples was first evaluated in vitro and benchmarked against pericytes grown in 2D or within 3D bulk hydrogels. To quantitatively assess protein changes that may reflect variations in cellular behavior across different culture conditions and to achieve detailed molecular insights at the proteome level, we applied advanced mass spectrometry–based proteomics to analyze pericyte-based myo-substitutes. The proteomic analysis revealed that the 3D culture environment promotes lower levels of mitogenic activity and downregulates adhesion-related molecular pathways compared to 2D cultures, supporting the formation of contractile, functionally mature bundles of pericyte-derived myotubes. Moreover, the biofabricated myo-substitutes showed a significant upregulation of both muscular matrix structural and contractile machinery proteins with respect to 3D bulk cultures. Finally, to demonstrate the robustness of the proposed strategy, biofabricated myo-substitutes were implanted into a mouse model of muscle volumetric damage, demonstrating their capability to graft and restore muscle architecture.

Altogether, our results highlight that biofabrication strategies may represent the next golden standard for the recapitulation of the SM architecture, and, more generally, for the assembly of functional artificial muscle substitutes.

2 | Results

2.1 | Microfluidic-Assisted 3D RoWS Biofabrication

To produce highly aligned muscle fibers from myogenic competent human pericytes (hPeri), we developed and validated a new biofabrication platform to reproduce such complex architectural organization. The system leverages the principles of wet-spinning technologies for the continuous, volumetric production of hydrogel fibers (Figure 1A). Contrary to conventional extrusion systems, our RoWS biofabrication platform is composed of just two axes: one linear (Figure 1A, *x*-axis arm) for the translational movement of the printing head and one rotary for the collection of the wet-spun fibers. A core part of the whole system is represented by the wet-spinning microfluidic printing head (ws-MPH). Specifically, we designed such a microfluidic device to enable the continuous production of core–shell hydrogel fibers (Figure 1B). To this aim, the MPH is equipped with a coaxial extrusion nozzle, which is placed at the bottom of a crosslinking bath microtank. Core and shell hydrogel precursor solutions are supplied, respectively, to the inner and outer nozzles of the coaxial system through a network of microchannels embedded in the microfluidic device. This configuration enables the formation of a stable coaxial flow of the two solutions within the nozzle, which, upon extrusion in the bath microtank, undergoes instantaneous gelation, resulting in a core–shell hydrogel fiber. Notably, the direct mounting of a crosslinking bath microtank over the ws-MPH not only significantly reduces the overall dimension of the wet-spinning printing head but also greatly simplifies the production and deposition of core–shell fibers, as it removes the need of using multiaxial nozzles and the supply of a third solution to crosslink the core–shell fiber.

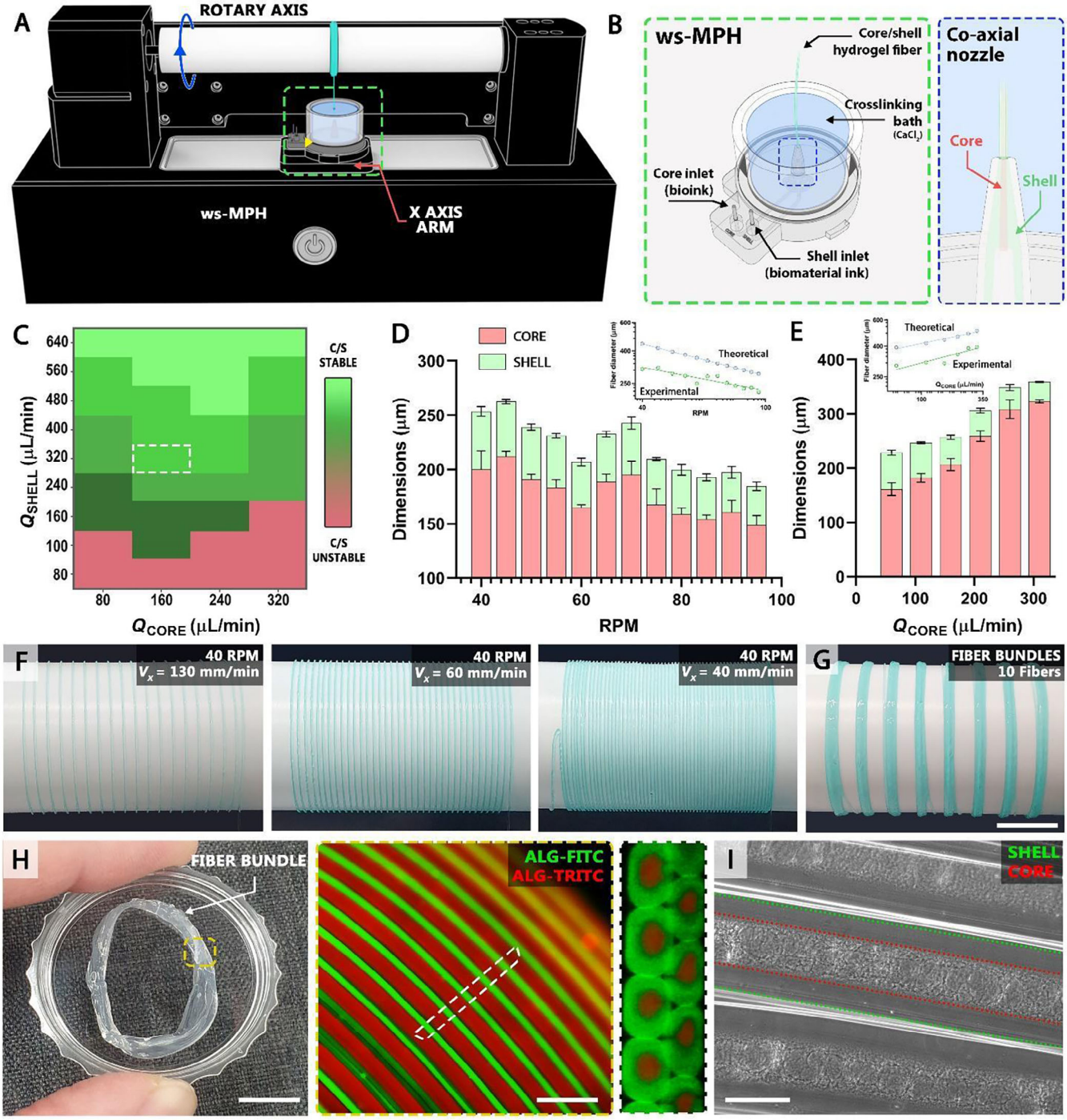

FIGURE 1 | Microfluidic-assisted 3D rotary wet-spinning (RoWS) biofabrication. (A) Schematic representation of the 3D RoWS biofabrication platform and (B) the coaxial microfluidic printing head (MPH) used to manufacture core–shell hydrogel fibers. (C) Stability diagram displaying the Q_{SHELL} and Q_{CORE} values suitable for continuous fiber spinning. (D) Influence of rotational speed over the size of extruded fibers (Q_{SHELL} = 320 µL/min and Q_{CORE} = 160 µL/min). (E) Effect of different Q_{CORE} over core–shell dimensions, keeping constant Q_{SHELL} (320 µL/min) and the rotational speed (64 rpm). Insets in (D) and (E) highlight the difference between theoretical and experimental values of fiber sizes, most likely caused by alginate gel shrinking upon crosslinking. (F) Various spiral fiber patterns obtained for different translation speeds and (G) assembly of fiber bundles with a specific number of fibers. (H, I) Bright field and fluorescence images of highly aligned fiber bundles characterized by a core–shell architecture. Scale bars: (H) (left) 5 mm, (right) 500 µm and (I) 250 µm.

Before starting the experiments with cells, we explored the full potential of our system by investigating the operational ranges where a stable production of core–shell fibers can be achieved. To this aim, we studied the influence of three main process parameters: the shell and core ink flow rates (Q_{SHELL} and Q_{CORE}) and the rotational speed used for fiber collection. During this preliminary characterization, the composition of the two inks was not varied. Respectively, the core bioink contained a semisynthetic biopolymer—namely PEG-fibrinogen (PF), at a concentration of 8 mg/mL—extensively used in SMTE [3, 17–21],

whereas the shell biomaterial ink was composed of a mixture of high and low molecular weight alginates—at a respective concentration of 10 and 20 mg/mL—to enable the immediate gelation with the Ca^{2+} ions contained in the microtank. Of note, we have experimentally found that human pericytes differentiate more efficiently in alginate-free bioinks, a feature in contrast with other recently published studies where murine progenitors necessitate the addition of 2 mg/mL of alginate in the core to prevent myotube collapse [19, 20].

The results of our preliminary system characterization are shown in Figure 1C–E. We first performed experiments at a constant rotational speed of 64 rpm to scan the effects of ink flow rates over fiber extrusion stability. A stable production of core–shell fibers can be achieved for a broad set of ink flow rates when the Q_{SHELL} is higher than 160 μL/min, whereas below such values, the fiber extrusion process resulted in flow instabilities, with frequent breakup of the extruded fibers. Accordingly, we selected as suitable values for the ink flow rates the pair $Q_{SHELL} = 320$ μL/min and $Q_{CORE} = 160$ μL/min. These values represent a proper trade-off between the high throughput, flow stability, and cell compatibility, namely minimizing the potential shear stress that cells could experience during extrusion at higher flow rates. Following these experiments, we characterized the influence of rotational speed over core and shell sizes using the selected pair of ink flow rates. The results revealed an opposite relationship, with faster rotational speeds causing the production of smaller fibers (Figure 1D). This can be explained by the fact that fibers collected on a drum that rotates faster will undergo a higher level of stretching. Additionally, we characterized the effect of different Q_{CORE} over core–shell dimensions, keeping constant Q_{SHELL} (320 μL/min) and the rotational speed (64 rpm).

As shown in Figure 1E, an increase of Q_{CORE} alone results in fibers having larger cores and thinner shells. Interestingly, the experimental values of fiber diameter were consistently lower than predicted theoretical values. This observation—where the experimental and theoretical data are plotted in a log–log space forming two parallel lines—seemed unrelated to the rotational speed (Figure 1D, insert) or the Q_{CORE} (Figure 1E, insert), and it was likely caused by gel shrinking effects that occur during the crosslinking of alginate solutions.

After the fiber extrusion parameters were evaluated, we proceeded with testing the capacity of our RoWS system in terms of the precision of the fiber spatial deposition. Notably, the developed custom user interface enables to independently control the *x*-axis motion and the rotational speed, allowing the creation of less or more densely packed spiral patterns of fibers that can be used to form thicker, rod-shaped 3D fiber constructs (Figure 1F). In this study, however, we focused on the production in series of bundles composed of highly anisotropic, compartmentalized hydrogels composed of core–shell fibers (Figure 1G) as these closely resemble SM architecture. As shown in Figure 1H, the fabricated bundles demonstrate structural stability, allowing for easy removal from the collecting drum. Additional rheological, mechanical, degradation, and swelling data for the precursor solutions and the obtained fiber structures are provided in Figure S1. Fibers within the bundles are tightly packed and aligned with a distinct and precise core and shell spatial compartmentalization. Of note, the latter can also be observed using phase contrast light when the core and shell hydrogels have either different chemical compositions (i.e., different optical densities) or different microstructures as in the case of fibrous fibrin core and smooth alginate shell (Figure 1I).

2.2 | From 2D to 3D Biofabrication: Promoting In Vitro Human Pericytes Myogenic Structuration

To evaluate the capacity of the proposed biofabrication system in guiding, on a large scale (i.e., centimeter scale), the myogenic differentiation of freshly harvested SM-derived human pericytes (hPeri), we defined and benchmarked three experimental groups: (i) a 2D standard cell culture system; (ii) a 3D soft, bulk hydrogel; and (iii) 3D-biofabricated constructs. The first two groups have been selected as they represent distinct culturing conditions largely employed and characterized among the SM research community [22, 23], thus being proper references to investigate whether a structurally and functionally improved muscle architecture can be obtained using our own biofabrication strategy.

Thus, we ran in parallel a series of experiments where hPeri structural organization and myogenic differentiation were first assessed using phase contrast and confocal microscopy. For all 3D experiments (i.e., bulk and biofabricated fibers), we used a photocurable hydrogel matrix, PEGylated-fibrinogen (PF), which is a semisynthetic biopolymer with exceptional capacity in supporting the in vitro differentiation of SM progenitors (Figure S2) [2, 3, 17, 18, 22]. The hPeri showed a pronounced differentiation in all the investigated groups as can be observed in Figure 2A–F, with the formation of multinucleated myotubes highly positive for myosin heavy chain (MyHC, a key muscle marker demonstrating advanced myogenic differentiation). However, the structural and spatial organization of these myotubes was significantly different among the three groups. In the 2D cell culture group, the hPeri differentiated into a single monolayer of adjacent myotubes exhibiting a short-range, random spatial alignment (Figure 2A,D). In the 3D bulk hydrogel group, hPeri formed an entangled 3D network of myotubes with an overall isotropic spatial distribution (Figure 2B,E). In the 3D-biofabricated group, hPeri were highly viable (Figure S3) and developed into densely packed myotubes characterized by a unidirectional, long-range alignment (Figure 2C,F). Most likely, the primary factor contributing to the improved cellular organization in the 3D-biofabricated group is the cell confinement within an anisotropic environment (i.e., fiber cores) as the shear forces produced during fiber extrusion do not seem to induce either a preferential cell alignment (Figure S4) or an alignment of the core gel itself (see Figure 1I). The improved myotube alignment in the biofabricated group represents an important step toward mimicking the cellular organization of native SMs. This feature can be appreciated from the directionality analysis performed on confocal fluorescence images (Figure 2D–F). Whereas the 2D and 3D bulk gel groups showed localized or no alignment at all, respectively, the biofabricated myo-structures revealed significantly sharper distributions centered along the fibers' major axis. To condense such differences into a practical value, data obtained from directionality analyses were fitted with a circular orientation distribution function (CODF; see Section 4). Such a function contains a single fit parameter ε that behaves in a similar way to

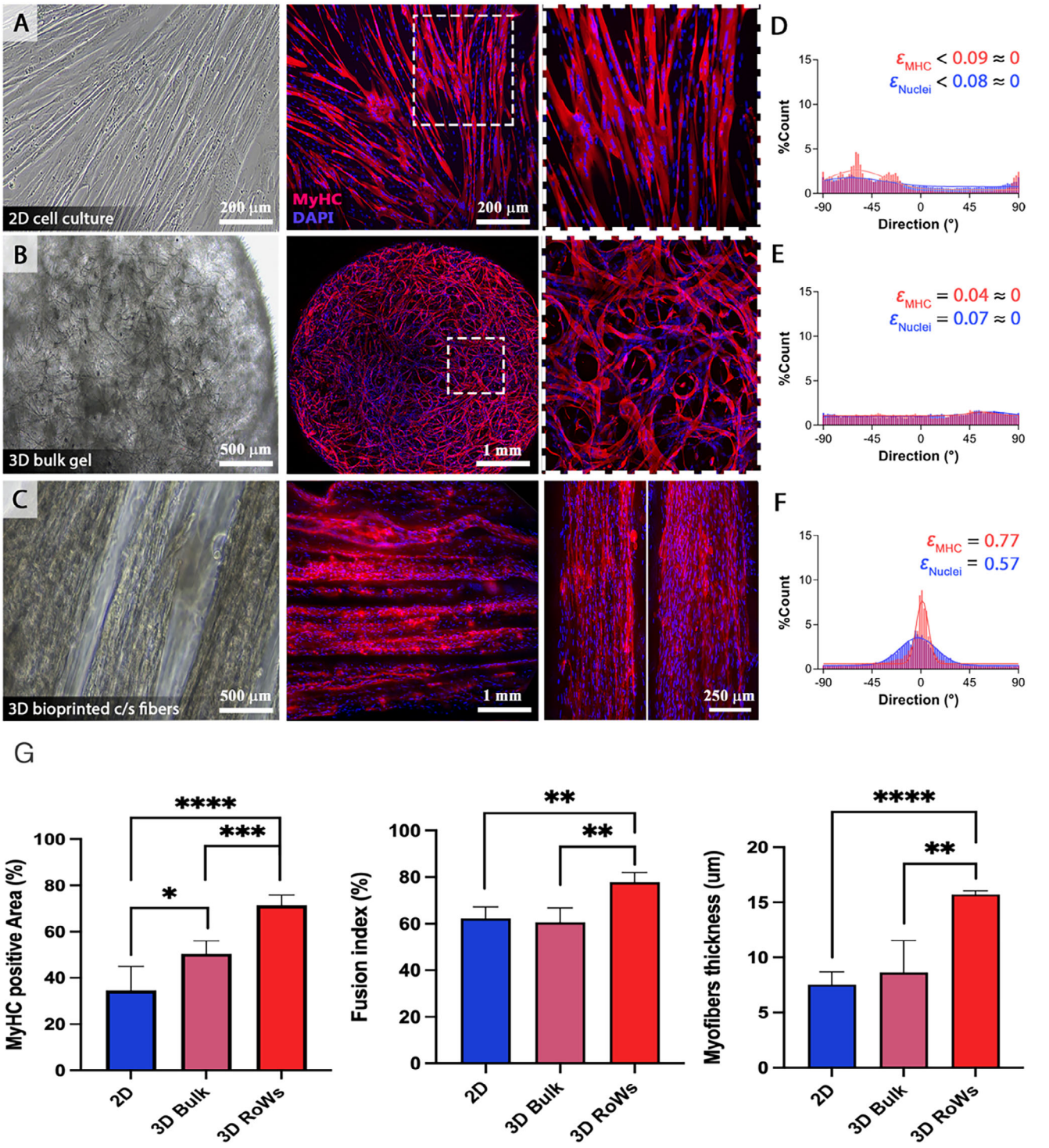

FIGURE 2 | In vitro human pericyte (hPeri) myogenic structuration in the three studied groups: 2D, 3D bulk gel, and 3D-biofabricated. (A–C) 2D, 3D bulk gel, and 3D-biofabricated core–shell fibers. Phase contrast and confocal images of hPeri cultured (A) on a 2D substrate, (B) in a 3D bulk gel, and (C) in 3D-biofabricated core–shell fibers (MyHC is shown in red, whereas DAPI staining is shown in blue). (D–F) Directionality analysis of the myo-structures obtained in the three studied groups. (G) Quantification of MyHC positive area, fusion index, and myofiber thickness illustrating the difference among the studied groups. Data are representative of at least three independent repeats. ****<0.0001; ***<0.002; **<0.01; *<0.05.

an *order parameter*: a value close to 1 indicates strong alignment, and progressively smaller values indicate lesser alignment (for a random sample, the scattering is isotropic and $\varepsilon = 0$). As expected, 2D and 3D bulk groups returned an ε value close to 0, whereas biofabricated samples, on the other hand, were characterized by significantly higher values ($\varepsilon_{MyHC} = 0.77$, $\varepsilon_{nuclei} = 0.57$), confirming their high degree of alignment. Moreover, in order to evaluate further differences in terms of muscle differentiation effectiveness among the three sample groups, MyHC expression area, fusion index, and myotube size have been analyzed (Figure 2G).

The results revealed a significant enhancement in the measured parameters for the 3D-biofabricated group, showing an increase of 20% in the MyHC positive area compared to the 3D bulk group and an even greater value in relation to the 2D. A similar performance has been registered as well in regard to fusion index and myotube size, respectively, displaying 20% and 50% amelioration of the 3D-biofabricated group versus 2D and 3D bulk ones. During differentiation, biofabricated constructs showed spontaneous, synchronous contraction of large sample areas, denoting a high level of maturation (Video S1). The spontaneous contractions of the biofabricated constructs were analyzed at different time points (Figure 3). As shown, the first spontaneous contractions occur after 5 days of culture until Day 20, in which the radial dispersion between the latency and the contraction phase reaches almost 30 μm. This spontaneous in vitro contraction in human-derived myogenic progenitors is generally hard to attain without externally applied mechanical or electrical stimuli [24]. Thus, these results provide a robust demonstration of the extent of myo-structure thoroughness achieved by the RoWS biofabrication approach.

2.3 | High-Resolution Mass Spectrometry–Based Proteomic

As shown, SM-derived human pericytes (hPeri) are a powerful source of competent myogenic precursor cells, and such myogenic potential is enhanced when culturing these cells in a 3D environment using PF matrix as the scaffold. However, mechanistic information on how the PF environment rewires these cells to form functional muscle bundles is currently missing. To pinpoint molecular details at the proteome resolution level, we decided to apply state-of-the-art mass spectrometry–based proteomics to dissect molecular information from pericyte-based myo-substitutes. Specifically, we selected ALP + hPeri from the SM biopsies of four healthy donors to establish primary cultures of such progenitors. Next, for each donor, we differentiated hPeri into mature myotubes by culturing these cells either in standard 2D cultures, in 3D bulk hydrogels, or in 3D-biofabricated aligned fibers via our custom core–shell 3D RoWS platform (Figure 4A). After 20 days, the hPeri gave rise to elongated MyHC-positive syncytia (as shown in Figure 2) that were harvested and subjected to standard lysis procedures. Solution digestion coupled with a label-free liquid chromatography (LC)-MS/MS quantitation approach [25, 26] allowed us to quantitate ~3200 proteins (Table S1). Proteome measurements were highly accurate and reproducible with a Pearson correlation (PC) coefficient among biological replicates ranging between 0.84 and 0.98 (Figure S5A). Principal component analysis (PCA) revealed that the proteome profiles efficiently discriminate different samples according to their culture conditions (Figure 4B). The drivers of the separation between 2D cultures and 3D constructs (Component 1 of the PCA loadings) were significantly enriched (FDR < 0.05) for muscle- and extracellular matrix–related terms (Table S2), confirming that 3D culture conditions favor differentiation and maturation of hPeri into contractile competent myofibers (Figure 4C).

The PF matrix profoundly changes the proteome of differentiated pericytes. Approximately 61% of the proteome of hPeri differentiated in bulk hydrogel constructs was found to be significantly different (FDR < 0.01) when compared to cells differentiated

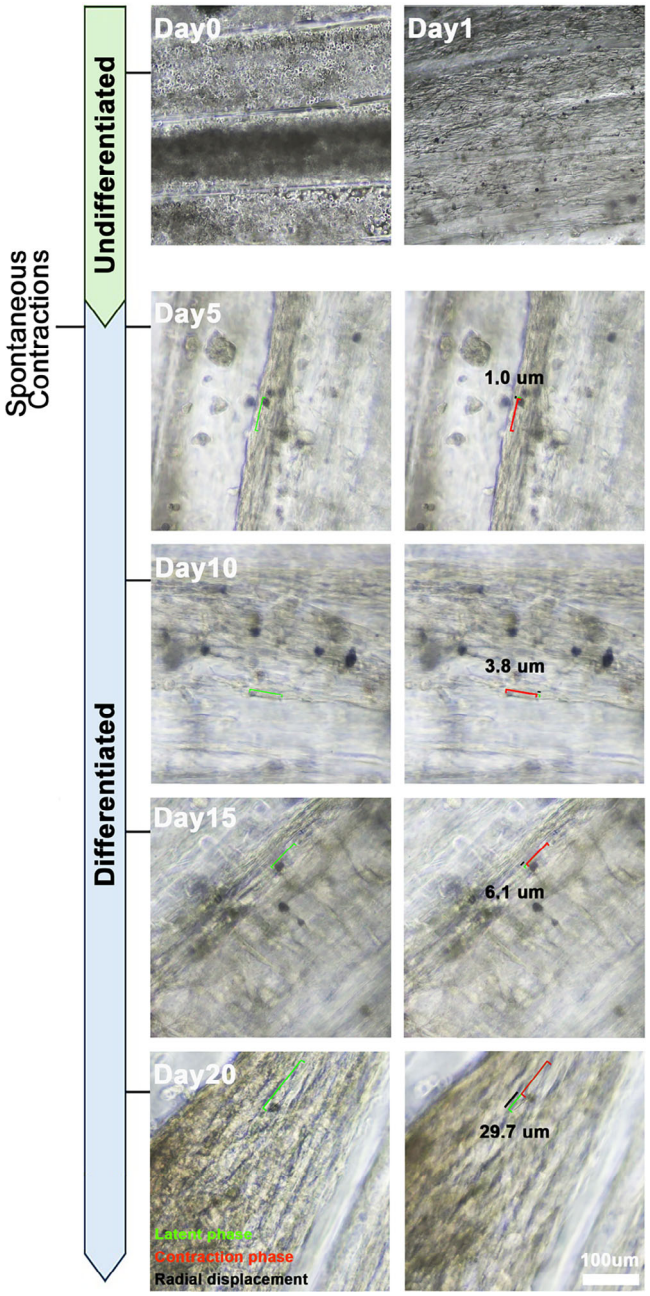

FIGURE 3 | Image analysis of spontaneous myotube twitching in biofabricated fibers. Representative bright field images obtained from spontaneous twitching videos showing the displacement of a reference segment during fiber contraction within biofabricated structures at different time points (full video frames are included as Supporting Information videos).

in 2D culture, allowing the identification of 1956 differentially regulated proteins (471 upregulated and 1485 downregulated, Figure S5B; Table S3). A slightly pronounced effect was found for hPeri differentiated in 3D-biofabricated fibers where proteome changes approach ~66% (FDR < 0.01, 729 upregulated and 1407 downregulated, Figure S5B; Table S3).

PC coefficient between the proteome comparisons (bulk-vs-2D and biofabricated-vs-2D) approaches 0.7 (Figure S5C) and includes 1577 significant proteins (Table S4) that are shared in

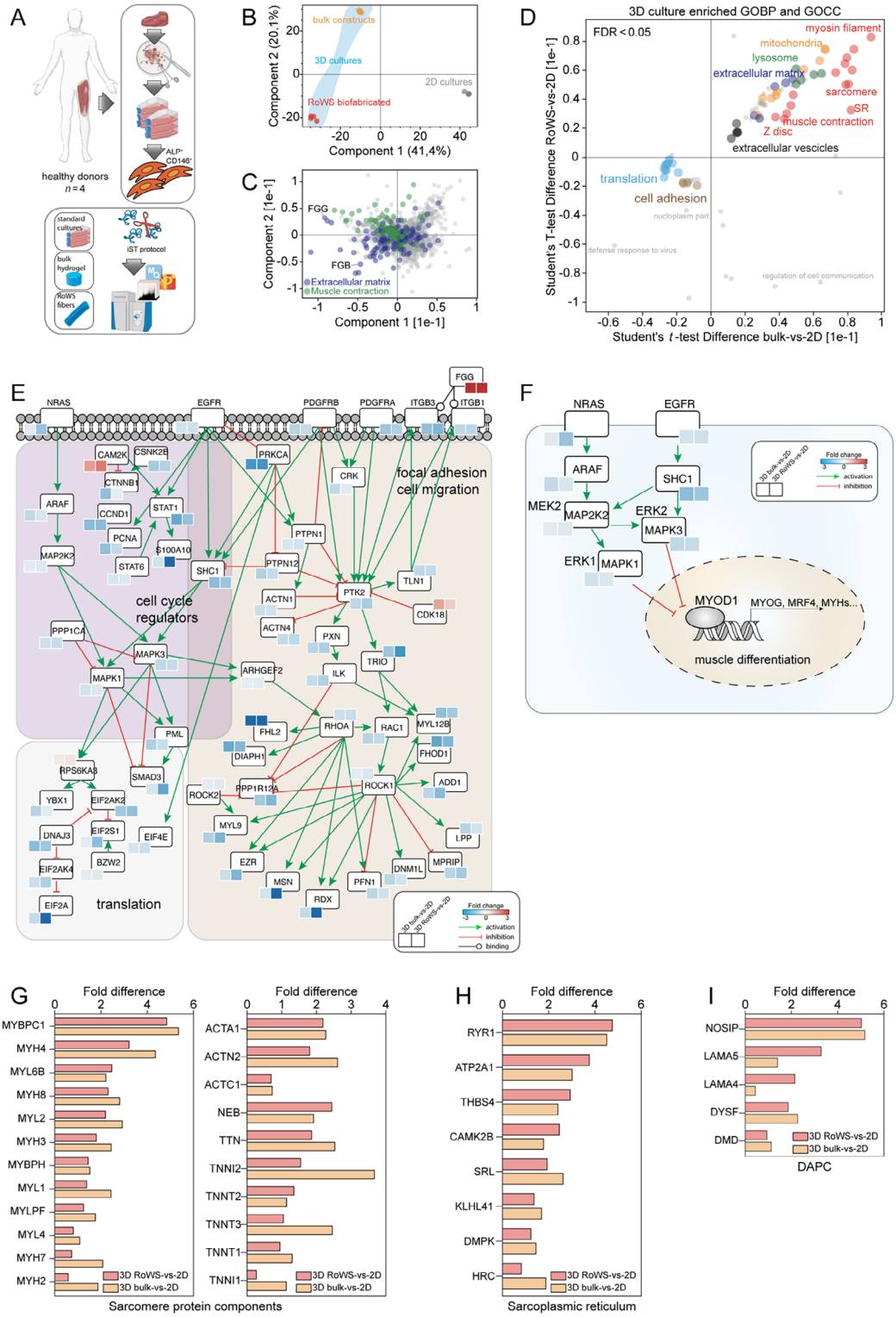

FIGURE 4 | High-resolution proteomics unravels the proteomic asset of 2D- and 3D-cultured human pericytes. (A) Representative scheme summarizing the proteomic workflow. (B) Principal component analysis (PCA) showing sample grouping across the considered experimental conditions. (C) Scatter plot showing the major protein determinants driving sample segregation in the PCA plot. Proteins belonging to the extracellular matrix are highlighted in blue, whereas those associated with muscle contraction are reported as green dots. (D) Two-dimensional annotation enrichment analysis of the significantly modulated proteins in biofabricated/2D (*y*-axis) and bulk/2D (*x*-axis). Groups of related GO terms are labeled with the same color, as described in the inset. (E) Casual network summarizing the main molecular events occurring in human pericytes upon 3D differentiation. (F) Casual network reporting signaling relationship between mitogenic pathways and MYOD1. (G) Bar plot reporting the fold difference (3D-biofabricated-vs-2D-cultured and 3D-bulk-vs-2D-cultured) of proteins annotated as "sarcomere protein components". (H) Bar plot reporting the fold difference (3D-biofabricated-vs-2D-cultured and 3D-bulk-vs-2D-cultured) of proteins annotated as "sarcoplasmic reticulum". (I) Bar plot reporting the fold difference (3D-biofabricated-vs-2D-cultured and 3D-bulk-vs-2D-cultured) of proteins annotated as "DAPC".

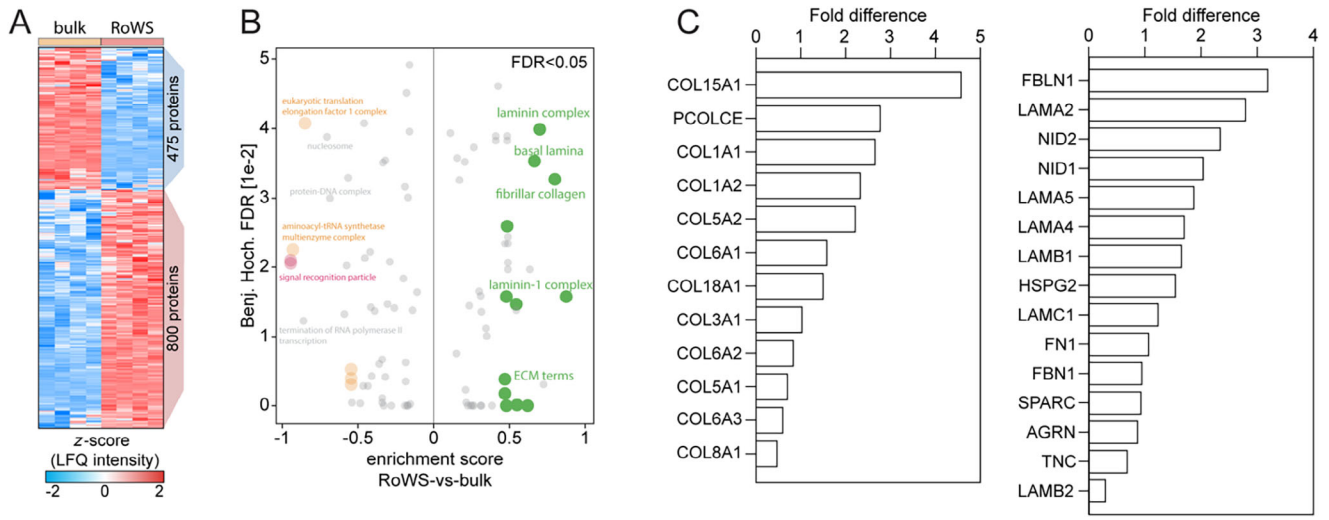

FIGURE 5 | 3D-biofabricated hPeri are stimulated to create the muscle microenvironment. (A) Heatmap showing significantly modulated proteins in the 3D-biofabricated RoWS-vs-3D bulk comparisons. (B) One-dimensional annotation enrichment analysis of the significantly modulated proteins (up- and down-regulated) in 3D-biofabricated-vs-3D bulk comparisons. GOBP terms are reported and those belonging to the same biological context are marked with the same color. (C) Bar plots reporting the fold difference in the 3D-biofabricated-vs-3D bulk comparisons of proteins annotated in the GO library as "collagen" and "extracellular matrix constituent". Proteins are ranked on the basis of their fold difference.

both groups (Figure S5D), suggesting that, independently from the degree of organization, the PF hydrogel matrix may exert a conserved impact on pericyte cells. To investigate this conserved effect, we used the 2D annotation enrichment analysis [27] to classify processes and compartments that were significantly (FDR < 0.05) represented/depleted in hPeri when differentiated in a PF hydrogel environment (Figure 4D; Table S5). According to the gene ontology (GO) library, muscle-specific processes (red dots), mitochondria- (yellow dots), lysosome- (green dots), extracellular matrix-terms (purple dots), and extracellular vesicles were found overrepresented on hPeri differentiated in a PF-rich environment, whereas processes associated with cell adhesion and translation were among the most depleted terms (Figure 4D).

To rationally classify the content of information of our proteomic survey, we mapped the shared 1577 significantly modulated proteins onto a literature-derived network of signaling and physical interactions extracted from the SIGNOR database with the aim to draw a PF-specific network. The resulting network encompasses 198 nodes including receptors and signal transducers while relationships between nodes are either positive (activations) or negative (inhibitions). Specifically, this strategy revealed that, in pericyte-derived myotubes, mitogenic pathways (RAS, EGFR, PGDFRA, and PDGFRB) as well as focal adhesion components (ITGB1, ITGB3, and PTK2) and cytoskeleton remodeling protein effectors (ROCK1, RHOA, and RAC1) were negatively affected in concentrations by the physical constraints created by the PF matrix (Figure 4E). To explain how such intracellular assets may contribute to stimulate pericyte myogenesis, we applied a transcription factor (TF) enrichment analysis (Table S6) to identify candidate myogenic downstream regulators that are sensitive to such a low mitogenicity environment (Figure S5E). We found that in both comparisons (bulk-vs-2D and biofabricated-vs-2D), the upregulated proteins were significantly enriched for all the members of the myogenic regulatory factors (MRFs), including MYOG, MYOD1, MYF6, and MYF5 that were among the top 10-ranked TFs (Figure S5E). Mitogenic pathways including RAS-RAF-MAPK and EGFR signaling repress myogenic differentiation by inhibiting these TFs, especially MYOD and MYOG to ensure the efficient expansion of the myoblast pool [28, 29] (Figure 4F). Consistently, the PF matrix depresses such constraints by massively inducing the expression of all sarcomere proteins including myosin, actin, and troponin isoforms (Figure 4G). Late myogenic genes, including sarcoplasmic reticulum proteins (Figure 4H) and components of the dystrophin-associated glycoprotein complex, were also increased in PF constructs (Figure 4I). Hence, for the very first time, our results demonstrated that the PF matrix confers a low mitogenicity environment that favors, in an anchoring-independent 3D state, the myogenic program stimulating the formation of contractile-competent bundles into pericyte-derived myotubes.

2.4 | 3D-Biofabricated Pericyte-Derived Myo-Substitutes Are Stimulated to Create the SM Niche

When extruded with the core–shell systems, pericyte cells are physically constrained to differentiate in highly aligned fibers, facilitating bundle orientation and myotube maturation. By contrast, bulk constructs gave rise to randomly oriented mature myotubes. To uncover molecular differences coming from the two selected strategies, we compared the proteome profiles collected from the 3D bulk and 3D-biofabricated samples. Such an approach identified 1275 significantly regulated proteins (FDR < 0.01, 800 upregulated and 475 downregulated proteins, Figure 5A; Table S7). We used the one-dimensional (1D) annotation enrichment analysis to identify significantly (FDR < 0.05) enriched processes in the considered comparison (Figure 5B; Table S8).

According to the GO library, basal lamina- and ECM-related terms (green dots) were the most enriched terms that describe

differences among 3D bulk and 3D-biofabricated constructs (Figure 5B). Consistently, collagen and fibrillar components are largely induced in biofabricated fibers (Figure 5C). This suggests that in this physically constrained environment, pericytes are stimulated to produce basal lamina components that act as a scaffold for pericyte myogenesis, thereby recreating the physiological SM fiber niche. Thus, besides the effect of 3D PF environment increasing the differentiation efficacy of hPeri by promoting the formation of contractile-competent bundles, the biofabrication strategy remarkably affects hPeri myogenic outcomes by stimulating the production of ECM-specific components (laminin [LAM], basal lamina, LAM-1 complex, etc.), which are fundamental for establishing the physiological architecture of SM tissue (Figure 5C). It can be observed that the differences between bulk and printed structures in terms of fold increase display a remarkable enhancement in ECM proteins, their interactors (Nidogen family, NID1, 2; heparan sulfate proteoglycan 2, HSPG2) and stabilizers (Fibrillin1, FBN1), providing a well-structured environment that supports muscle differentiation and maturation. It is noteworthy that, despite the negative impact on focal adhesion components observed in the 3D environment, the 3D-biofabricated myo-substitutes demonstrate a positive effect on ECM-interacting proteins, promoting basal lamina and LAM cell adhesion, as shown by collagen Type XV alpha 1 chain (COL15A1) and fibulin 1 (FBLN1) increase (Figure 5C).

2.5 | hPeri-Derived 3D-Biofabricated Myo-Substitute Implantation Into a Volumetric Muscle Loss (VML) Mouse Model

We ultimately evaluated the potential of our biofabrication strategy by grafting human pericyte-derived myo-substitutes into a VML animal model. Prior to transplantation, we ensured that the 3D-biofabricated myo-substitutes exhibited essential characteristics, including the production of matrix, sarcomeric proteins, and muscle-specific proteins. Our VML mouse model consisted of the surgical removal of 30% of the tibialis anterior (TA) muscle, following a *tried-and-true* protocol [2, 18] (Figure 6). The chosen degree of muscle ablation (30%) aimed to avoid xenograft issues, as even immunocompromised mouse strains still possess active macrophages that may rapidly invade the ablated TA and target *non–self*-cells. Moreover, the selection of the damage size for VML modeling was based on previously published data, which reported the critical size of muscle defect in order to generate a reliable VML damage model [2, 18, 30, 31]. The hPeri-derived myo-substitutes were grafted into the site after being appropriately trimmed to fit the TA lodge created by the removed muscular tissue. The contralateral TA served as the sham control. After a 30-day-period postimplantation, the sham control group showed no signs of regenerating or replenishing tissue in the damaged area, as depicted in Figure 6B,C. In contrast, the TAs that had been treated with the RoWS-biofabricated structures exhibited evidence of hPeri-derived regenerating tissue, as observed in Figure 6D,E. The center-nucleated muscle fibers within the regenerated tissue displayed positive staining for the human-specific markers lamin A/C and myosin heavy chain (as indicated by the arrows in Figure 6F,G). These results highlight the ability of the hPeri-biofabricated myo-substitute to produce muscle tissue capable of replacing the removed TA mass and closing the gap created by the VML. Furthermore, we assessed the vascularization potential of the RoWS-generated myo-structures by performing immunofluorescence staining against the vessel-specific marker smooth muscle actin (SMA), which labels the blood vessel wall. The immunofluorescence images, shown in Figure 6H–I, provided insights into the engraftment capability of the RoWS-generated structures, confirming the presence of a neo-vascularization process within the repaired tissue.

The regenerating area showed a remarkable recruitment of SMA-positive blood vessels, pivotal for the engraftment and survival of the implanted myo-substitute. In the enlarged view of the grafted area, it is appreciable that infiltration of small and larger vessels was evident (Figure 6H,I). Quantitatively assessing the vascularization using ImageJ software was carried out to demonstrate vessel colonization in the pericyte-derived reconstructed muscle tissue. The results show an approximately twice higher SMA-positive area in the treated muscles when compared with the undamaged TA area used as a control (Figure 6J). Further analyses were performed to support engraftment capability of the RoWS-generated myo-substitute, exploiting platelet endothelial cell adhesion molecule (PECAM-1), also known as CD31, immunoreaction against vessel endothelial cells (Figure S6A,B) and anti-neurofilament (NF) and bungarotoxin to label axons and neuromuscular synapses (Figure S6C,D). The so-stained implanted area revealed the recruitment of vessel and axons reestablishing the NMJ positive for BTX. Furthermore, the number of CD31 positive vessels was evaluated by counting the number of CD31+ structures in the implanted area compared with the undamaged control muscle, showing no significant difference (Figure S6E). These results are in line with our previous findings [2], demonstrating the proper establishment of a neo-vasculature within the graft volume. The neo-vascularization process occurring in the treated TA muscles may find a partial explanation in our proteomic survey. In fact, 3D-biofabricated hPeri significantly upregulated a panel of molecules annotated as angiogenic factors, including CHI3L1, SERPINF1, and THBS4 (Figure S6F; Table S9). We speculate that the upregulation of such factors may contribute effectively to the recruitment of blood vessels, thereby leading to better integration with the host TA muscle and eventually generating human-derived myofibers in the mouse muscle.

3 | Discussion

SM tissue is a peculiar example of how intertwined the structural and functional properties of a tissue can be, from the molecular level up to the macro scale. Regrettably, such orchestrated organization is lost in several debilitating conditions including traumatic injuries, invasive surgeries, or devastating muscle diseases. In those cases, the massive removal/wasting of functional muscles (i.e., VML) is not compensated by the intrinsic regenerative potential of this tissue. Fortunately, current advances in biotechnology and bioengineering are paving the way for a new regenerative era. Novel platforms and bioengineered products [32] (e.g., bioreactors, organoids, organs-on-a-chip, and bioprinting systems) are opening an unprecedented level of possibilities to generate miniaturized, and, in most cases at actual scale, functional organ/tissue models that can be used to treat or to replace the damaged ones. In the case of muscle biology, the major challenge is to develop and validate a bioengineering system capable

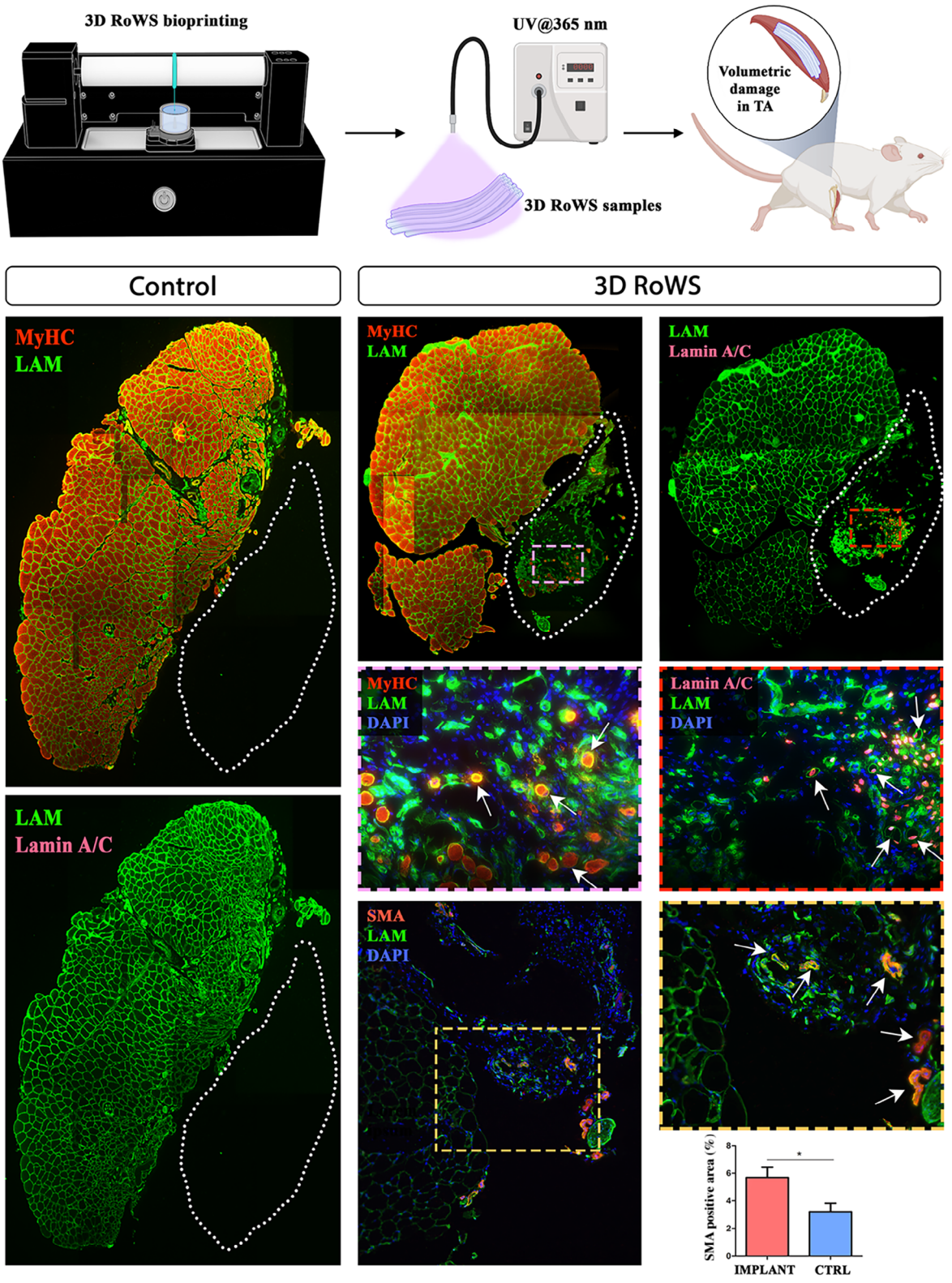

FIGURE 6 | hPeri-derived 3D-biofabricated myo-substitute engraftment into a mouse TA volumetric damage. (A) Schematic representation of the 3D RoWS-derived myo-substitute implantation. Reconstructed TA cross-sections from (B, C) sham (control) and (D–I) implanted (treated with 3D-biofabricated myo-substitutes) mice; immunofluorescence against myosin heavy chain (MyHC), laminin (LAM), and human lamin A/C (lamin A/C). (F, G) Enlarged views of selected areas, respectively, from (D) and (E). (H) Smooth muscle actin (SMA) immunostaining at the interface between implant and host native muscle demonstrating the neo-vascularization process occurring in the implanted mice. (I) Magnification of a selected area from (H) showing the 3D RoWS-derived myo-substitute integration in the host muscle tissue. (J) Quantification of SMA positive areas in the cross-sections obtained from the implant and control samples. Scale bars: (B) 150 μm; (D) 200 μm; (F, G, I) 50 μm; and (H) 100 μm.

of reproducing the complex native architecture and composition, including the hierarchical compartments of connective tissue and muscle cells, while demonstrating the full biocompatibility and grafting of such constructs in host recipients.

To this end, in the present manuscript, we investigated whether 3D biofabrication technologies—in particular our RoWS platform—may enhance the maturation of SM human progenitors, possibly leading to more reliable and functional SM models. The proposed biofabrication strategy leverages wet-spinning principles to create anisotropic 3D constructs comprising densely packed, parallelly aligned hydrogel fibers. Through the incorporation of a custom microfluidic printing head, we achieved continuous fabrication of core–shell fibers. By leveraging our experience of optimizing the biochemical composition and mechanical properties of these fibers, we successfully supported a robust differentiation of human-derived SM progenitors, leading to the formation of well-organized myotubes and the expression of important marker proteins like MHC. The proposed system is highly scalable (it generally operates at the decimeter scale), and, with minimal adjustment, it may be used to manufacture relevant histomimetic constructs suitable for translation into the clinics. Moreover, as regards the microarchitecture and the degree of mimicry of our bundles with respect to native tissue, each of our fibers can be considered the equivalent of a muscle fascicle containing several myotubes, with the shell of each fiber mimicking the perimysium. At the same time, we speculate that the current fiber size (approx. 350 microns) efficiently supports the diffusion of the nutrients and oxygen to the growing myotubes, thus allowing us to maintain high cell viability in the decimeter-scale constructs.

For the very first time, we demonstrated by means of state-of-the-art mass spectrometry–based proteomics the effects that the 3D PF matrix provides to these cells, including a low mitogenicity environment and blocking of the cell adhesion machinery. These factors promote a myogenic program and facilitate the formation of contractile-competent bundles in pericyte-derived myotubes. Following in vitro investigation, we tested our biofabricated myo-substitutes within a VML animal model. The biofabricated structures revealed the ability to regenerate muscle tissue, as evidenced by the presence of hPeri-derived regenerating tissue containing positive markers for human-specific proteins and an overall ability to integrate with host muscular tissue. Vascularization and innervation assessment further demonstrated optimal grafting biocompatibility of RoWS-generated structures with the host recipients. Although the main limitation of this work is the absence of functional assessments of RoWS-generated structures, the spontaneous contraction ability of tightly packed myobundles infers an advanced myotube maturation of the 3D-biofabricated myo-substitutes.

In conclusion, we demonstrated that by exploiting RoWS biofabrication technology, one can obtain enhanced maturation and structural organization of human-derived muscle progenitors compared to 2D or 3D bulk gel models. Of note, by leveraging state-of-the-art proteomic analysis, we identified, at the molecular level, how the proposed biofabrication approach effectively modulates not only the differentiation and maturation of the arising myotube structures but also plays a role in the modulation of angiogenic pathways that may promote a better neovascularization and tissue engraftment upon implantation in vivo. The deployment of a 3D RoWS biofabrication strategy has proven effective for promoting myotube organization and maturation, as well as enhancing muscle-specific ECM protein production, as demonstrated by proteomic analysis. These results highlight the potential of this approach for developing a human myo-substitute of relevant size that could be used therapeutically in patients who have undergone muscle removal or experienced major trauma. To validate this potential, new experimental procedures are being tested in a larger mammal with physical characteristics similar to humans, aiming to gain fundamental insights into muscle repair and further demonstrate the efficacy of the proposed method.

4 | Materials and Methods

4.1 | Materials

Unless otherwise noted, all chemicals were obtained from Sigma-Aldrich and used directly. FMC biopolymers generously provided sodium alginates with low molecular weights (LMW-ALG, Mw 33 kDa) and high molecular weights (HMW-ALG, Mw 100 kDa). ALG-FITC and ALG-TRITC were synthesized following a previously published procedure [17].

PEG-diacrylate was synthesized as described elsewhere [33]. Briefly, linear PEG-OH with an average molecular weight of 10 kDa (Fluka, Buchs, Switzerland) was reacted with acryloyl chloride (Merck, Darmstadt, Germany) at a molar ratio of 1.5:1 relative to OH groups in dichloromethane (Aldrich, Sleaze, Germany) and triethylamine (Fluka, Buchs, Switzerland). The final product was precipitated in ice-cold diethyl ether (Frutarom, Haifa, Israel), followed by vacuum drying for 48 h. Proton-NMR (nuclear magnetic resonance) spectroscopy was used to quantify the degree of acrylation. The PF was prepared by conjugating PEG-DA with denatured, reduced fibrinogen chains by Michael-type addition, according to the previously described protocol [34]. Briefly, 7 mg/mL solution of bovine fibrinogen (ID bio, France) in 150 mM phosphate–buffered saline (PBS) containing 8 M urea was reacted with Tris (2-carboxyethyl) phosphine hydrochloride (TCEP–HCl) (Sigma–Aldrich) at a molar ratio of 1.5:1 to fibrinogen cysteines. Once the protein was dissolved, PEG-DA in a solution of PBS and 8 M urea (280 mg/mL) was added, in a molar ratio of 4:1, to initiate the PEGylation reaction. The reaction was carried out for 3 h at room temperature in the dark. Then, the PEGylated protein was precipitated by adding 4 volumes of acetone (Bio-lab) and was re-dissolved in PBS-Urea to the desired concentration, followed by dialysis (Spectrum 12–14 kDa MW cutoff, USA) against 150 mM PBS for 24 h at 4°C. Finally, the fibrinogen concentration in the product was measured by a NanoDrop spectrometer (A-280 nm, PF coeficiency-15.1) and the degree of PEG substitution was calculated according to published protocols [34]. Rheological parameters were calculated using a strain-rate–controlled shear rheometer (AR-G2, TA Instruments, Delaware, USA) with a parallel-plate geometry, as detailed elsewhere [35].

4.2 | 3D RoWS Biofabrication Setup

Using a customized 3D RoWS setup developed in our lab, core–shell hydrogel fibers were created and spatially deposited in three

dimensions. The entire platform includes an extrusion system made up of a rotating drum collector with a diameter of 20 mm and a length of 180 mm, an *x*-axis with a travel range of 160 mm, and a crosslinking bath microtank with a coaxial nozzle placed at the bottom for the immediate gelation of extruded core–shell fibers (inner needle diameter: 500 μm and outer needle diameter: 500 μm). Using an Arduino Mega board and specialized Python software, the entire system was controlled. Utilizing a transparent and class I biocompatible resin (Class I polymer for surgical guides as per Rule 5, Annex IX of Medical Devices Directive 93/42/EEC) and stereolithography 3D printing (DWS 3500PD), the microfluidic printing head was created. The nozzle was thoroughly rinsed in isopropanol to remove unreacted photoresin that was trapped in the channels after the 3D printing, dried, and then crosslinked for an additional 10 min in a UV curing oven. The 3D-printed MPH was then mounted on the *x*-axis arm of our RoWS system and given a crosslinking bath microtank.

4.3 | Human Pericytes (hPeri) Isolation Procedure and Culture

hPeri were isolated from muscle biopsies collected from healthy donors. Tissues were minced and then digested with 100 U/mL of collagenase Type II (Gibco, Life Technologies, Carlsbad, CA, USA) in PBS with Ca^{2+} and Mg^{2+}, for 60 min. Afterward, muscle fragments were gently dissociated by pipetting and passing through a 100 μm cell strainer. Cell suspension was centrifuged for 10 min at 1200 rpm, and the pellet was resuspended and filtered again with a 70 μm cell strainer. Cell suspension was then centrifuged for 10 min at 1200 rpm, and the pellet was resuspended and seeded in 100-mm Petri dishes at low confluences (1000 cells/cm^2) in CYTO-GROW medium (Resnova), supplemented with 100 IU/mL penicillin and 100 mg/mL streptomycin (Gibco). The cells were selected for their capacity to form colonies on plates that exhibited positive expression of alkaline phosphatase (AP) and other hPeri-associated markers [12]. The cells were expanded and cultured in 100-mm Petri dishes for further experimentation.

4.4 | In Vitro Analysis of hPeri Myogenic Structuration in 2D and 3D Culture Conditions

To study hPeri myogenic structuration, the cells were plated in 6-well Petri dishes (3×10^5) or used in bioink formulation with the aim to produce 2D cell culture, 3D bulk, and 3D RoWS-derived myo-constructs. hPeri-derived cultures were grown up to 21 days in CYTO-GROW (Resnova) supplemented with 100 U/mL penicillin and 100 mg/mL streptomycin (Gibco) at 37°C and 5% CO_2 humid atmosphere until reaching the complete differentiation condition.

4.5 | Fabrication of Human Pericyte–Loaded 3D Myogenic Structures

4.5.1 | 3D Bulk Structures

3D bulk hydrogels were fabricated by a casting method: human-derived pericytes 2×10^7 hPeri/mL were soaked into a sterile-filtered precursor solution made of 0.8% w/v PF in 25 mM HEPES buffer and 0.1% w/v Irgacure 2959 as radical photoinitiator. Afterward, the mixture was poured into cylindrical silicone molds (PDMS) and then exposed for 5 min to UV light for PF polymerization. The bulk structures were placed in CYTO-GROW (Resnova) supplemented with 100 U/mL penicillin and 100 mg/mL streptomycin (Gibco) at 37°C and 5% CO_2 humid atmosphere.

4.5.2 | 3D-Biofabricated Core–Shell Fiber Structures

The custom coaxial MPH was used to create core–shell hydrogel fibers. The core bioink contained 2×10^7 hPeri/mL suspended in a sterile-filtered solution containing 0.8% w/v PF in 25 mM HEPES buffer solution. To create the shell biomaterial ink, 2% w/v LMW-ALG and 1% w/v HMW-ALG were dissolved in 25 mM HEPES. The MPH and tubing were cleaned with a 70% ethanol solution prior to use and then flushed with sterile dH_2O. To create the co-flow in the extrusion nozzle, the inks were fed continuously into the MPH nozzle. The typical core and shell flow rates in all cellular experiments were $Q_{CORE} = 160$ mL/min and $Q_{SHELL} = 320$ mL/min. After that, 0.6 M $CaCl_2$ solution was added to the cross-linking bath microtank before the extrusion of the core and shell inks. Upon encountering $CaCl_2$, the core–shell fibers immediately begin to gel in the vicinity of the nozzle's tip. A tweezer is used to gently pull the hydrogel fiber that results up until it touches the Teflon drum's surface. A hydrogel fiber begins to continuously extrude from the nozzle and collect onto the drum in the form of a bundle as soon as the fiber contacts the drum. The drum's rotational speed was set to 64 rpm, and the number of threads in each bundle (37 threads per bundle, 30 s of extrusion) remained constant. The samples were taken from the rotating drum after extrusion. The bundles were exposed to 365 nm UV light for 5 min to crosslink the bioink in the core. Following this, the bundles were placed in CYTO-GROW (Resnova) supplemented with 100 U/mL penicillin and 100 mg/mL streptomycin (Gibco) at 37°C and 5% CO_2 humid atmosphere. Bundles were cultured in six-well plates.

4.6 | SM Organization Image Analysis

Thanks to its unique aligned architecture, we estimated the organization of SM artificial tissue in the studied groups by computing the directionality of immunofluorescence images using Fiji built-in plugin (https://imagej.net/plugins/directionality). Data obtained from directionality analyses were then fitted with a CODF, $((\theta) = (1 - \varepsilon^2)/[(1 + \varepsilon)^2 - 4\varepsilon \cos^2 \theta])$ where the single fit parameter ε behaves in a similar way to an order parameter: a value close to 1 indicates strong alignment, whereas progressively smaller values indicate lesser alignment. For a random sample, the scattering is isotropic and $\varepsilon = 0$. Interestingly, both 4′,6-diamidino-2-phenylindole (DAPI) and MHC channels were used in the analysis, providing insights about the alignment of nuclei and myotubes.

4.7 | Image Analyses

The evaluation of images was conducted utilizing the ImageJ/FIJI software. To summarize, we examined spontaneous twitching

in 3D-biofabricated constructs at different time points (5, 10, 15, and 20 days) by analyzing individual frames extracted from live-imaging recordings. Following image calibration, we measured the radial movement during twitching relative to a specific reference point within the image using the Straight Line function [3].

The myofibers thickness, CD31 positive vessel count, and fusion index were calculated in a 0.4 mm [2] ROI of the immunofluorescence image using the straight-line function and multipoint tool, respectively, after image calibration. For the SMA and MyHC positive area, the acquired fluorescent MyHC signal was converted to an 8-bit image and a threshold of 50 was applied to generate a binary image. After setting the scale and selecting the measurement of interest, the percentage of positive area was measured using the measure function [5].

4.8 | Proteome Sample Preparation

Samples were harvested and directly lysed in an ice-cold RIPA buffer. In-gel fractionation was performed via SDS-PAGE electrophoresis. Gel lanes were cut into equal pieces and digested. In brief, gel pieces were washed, destained, and dehydrated. Proteins were reduced with 10 mM dithiothreitol (DTT), alkylated with 55 mM iodoacetamide (IAA) and digested with the endopeptidase sequencing-grade Trypsin (Promega; Madison, WI, USA) overnight at 37°C. Collected peptide mixtures were concentrated and desalted using via in-StageTip (iST) method [36]. Samples were separated by high-performance LC in a single run (without prefractionations) and analyzed by LC-MS/MS.

4.9 | LC-MS/MS Measurements

Instruments for LC-MS/MS analysis consisted of a NanoLC 1200 (Thermo Fisher Scientific) coupled via a nano-electrospray ionization source to a quadrupole-based Q Exactive HF benchtop mass spectrometer (Thermo Fisher Scientific). Peptide separation was carried out according to hydrophobicity on a home-made column (75 µm inner diameter, 8 µm tip, and 400 mm bed packed with Reprosil-PUR, C18-AQ, 1.9 µm particle size, 120 Å pore size [New Objective, PF7508-250H363]), using a binary buffer system consisting of solution A (0.1% formic acid) and B (80% acetonitrile and 0.1% formic acid). The total flow rate was 300 nL/min. For the LC linear gradient, after sample loading, the run started at 5% buffer B for 5 min, followed by a series of linear gradients, from 5% to 30% B in 90 min, then a 10 min step to reach 50% and a 5 min step to reach 95%. This last step was maintained for 10 min.

MS spectra were acquired using 3×10^6 as an automatic gain control (AGC) target, a maximal injection time of 20 ms, and 120,000 resolution at 200 m/z. The mass spectrometer operated in data-dependent Top20 mode with subsequent acquisition of higher-energy collisional dissociation fragmentation MS/MS spectra of the top 20 most intense peaks. Resolution for MS/MS spectra was set to 15,000 at 200 m/z, AGC target to 1×10^5, maximum injection time to 20 ms, and the isolation window to 1.6 Th. The intensity threshold was set at 2.0×10^4 and dynamic exclusion at 30 s.

4.10 | Proteome Data Processing

All acquired raw files were processed using MaxQuant (1.6.2.10) and the implemented Andromeda search engine. For protein assignment, spectra were correlated with the Human (v. 2021) reference proteome, including a list of common contaminants. Searches were performed with tryptic specifications and default settings for mass tolerances for MS and MS/MS spectra. The other parameters were set as follows: fixed modification, carbamidomethyl (C); variable modifications, oxidation, acetyl (N-term); digestion, trypsin, Lys-C; minimum peptide length, 7; maximum peptide mass, 470 Da; and false discovery rate for proteins and peptide spectrum, 1%.

For further analysis, Perseus software (1.6.2.3) [27] was used and first filtered for contaminants and reverse entries as well as proteins that were only identified by a modified peptide (first filter). The label-free quantitation (LFQ) ratios were logarithmized, grouped, and filtered for minimum valid number (minimum of three in at least one group) (second filter). Missing values were replaced by random numbers drawn from a normal distribution. Two-sample t-test analysis was performed using S0 = 0.1 FDR < 0.01. Proteins with $\log_2$ difference $\geq \pm 1$ and $q < 0.01$ were considered significantly enriched. Categorical annotation was added in Perseus in the form of GO biological process, GO molecular function, and GO cellular component, and Kyoto Encyclopedia of Genes and Genomes (KEGG) pathways.

4.11 | Protein Network Generation

This strategy has been previously developed and applied to query complex muscle-specific proteome datasets [37]. Casual relationships between significant protein entities were retrieved from the SIGNOR database [38] using a dedicated application in the Cytoscape platform [39]. Nodes were color coded according to their difference value in the dedicated comparison.

4.12 | In Vivo 3D RoWS-Derived Myo-Substitute Implantation in a VML Mouse Model

Two-month-old male SCID/Beige mice were anesthetized with an intramuscular injection of physiologic saline (10 mL/kg) containing ketamine (5 mg/mL) and xylazine (1 mg/mL), and then the 3D RoWS-derived myo-constructs were implanted in TA muscle of a VML mouse model recreated according to following surgical procedure [2, 18]: (i) To get as far as the TA, a confined incision on the medial side of the leg has been executed, (ii) the muscle fibers were deeply removed (leaving in place the tendons) by employing a cautery to avoid bleeding and to create an adequate shelter for the implant, and (iii) the biofabricated myo-substitute was positioned in the removed TA fibers lodge and the incision was sutured. In the contralateral TA, used as a control, no construct was implanted; it was only surgically ablated and sutured to produce VML damage.

Analgesic treatment (Rimadyl, Pfizer, USA) was administered after the surgery to reduce pain and discomfort. Mice were sacrificed 30 days after implantation for molecular and morphological analysis. Experiments on animals were conducted according to

the rules of good animal experimentation I.A.C.U.C. no. 432 of March 12, 2006, and under Italian Health Ministry approval no. 228/2015-PR.

4.13 | Immunofluorescence

Following in vitro culture, 2D, 3D bulk, and 3D RoWS-derived myo-constructs were fixed in 2% PFA and processed for fluorescence microscopy as previously described [18].

The in vitro constructs were incubated with anti-myosin heavy chain (MHC, Clone MF20 DSHB, 1:50 titer). Samples were counterstained with DAPI to detect nuclei and mounted on glass slides with glycerol to be imaged with Nikon A1R laser scanning confocal microscope with the NIS software.

Conversely, constructs explanted from SCID mice were embedded in O.C.T. and quickly frozen in liquid nitrogen–cooled isopentane for sectioning at a thickness of 8 mm on an EPREDIA cryostat. Sections were permeabilized with 0.3% Triton X-100 in PBS for 30 min and blocked in blocking solution formed by 10% of goat serum, 1% of glycine, 0.1% Triton X-100 in PBS for 1 h at RT. Subsequently, sections were incubated with primary antibody in blocking solution for 2 h at RT. Primary antibodies were diluted as follows: mouse monoclonal anti-myosin heavy chain (MHC; Clone MF20 DSHB) 1:2, rabbit polyclonal anti-LAM (Sigma-Aldrich) 1:200, mouse monoclonal anti-α-SMA (Sigma-Aldrich) 1:100, rabbit polyclonal anti-von Willebrand factor (vWF, Abcam) 1:100, mouse monoclonal anti-lamin A/C (Thermo Fisher Scientific) 1:200. After several washes with washing solution formed by 1% BSA and 0.2% Triton X-100 in PBS, sections were incubated with Alexa Fluor 555-conjugated goat anti-mouse IgG (H+L; Thermo Fisher Scientific, 1:400) and Alexa Fluor 488-conjugated goat anti-rabbit (H+L; Thermo Fisher Scientific, 1:400) in blocking solution for 1 h at RT. Samples were counterstained with DAPI to detect nuclei, washed three times with PBS, and mounted on glass slides with Vectashield mounting medium (Vector Laboratories). Samples were imaged with a Nikon Eclipse TE2000 microscope equipped with a CoolSNAP MYO CCD camera (Photometrix) and MetaMorph software.

4.14 | Statistical Analysis

The data were analyzed using GraphPad Prism 9, and values were expressed as means ± standard error of the mean (SEM). Statistical significance was assessed using either a two-way ANOVA with Tukey's post hoc test or a *t*-test when only two parameters were compared. A p value of less than 0.05 was considered statistically significant.

Author Contributions

Alessio Reggio: conceptualization, methodology, investigation, writing the original draft preparation, writing and revising the final manuscript. **Claudia Fuoco:** conceptualization, methodology, investigation, writing the original draft preparation, writing and revising the final manuscript. **Francesca De Paolis:** validation and formal analysis. **Rebecca Deodati:** validation and formal analysis. **Stefano Testa:** methodology. **Nehar Celikkin:** methodology. **Marina Volpi:** methodology, validation. **Sergio Bernardini:** formal analysis. **Ersilia Fornetti:** methodology. **Jacopo Baldi:** resources. **Roberto Biagini:** resources. **Dror Seliktar:** resources. **Carmine Cirillo:** proteomic data analysis. **Wojciech Swieszkowski:** metodhology, revising final manuscript. **Paolo Grumati:** proteomic data analysis, methodology, revising the final manuscript. **Stefano Cannata:** project administration, methodology. **Marco Costantini:** methodology, investigation, writing and revising the final manuscript, project administration and funding acquisition. **Cesare Gargioli:** conceptualization, methodology, writing and revising the final manuscript, project administration and funding acquisition.

Acknowledgments

This work was supported by AFM-Téléthon (23551 to A.R.), Fondazione Telethon (TMPGMFU22TT to P.G.), Muscular Dystrophy Association (MDA 968551 to P.G.), National Science Centre Poland (NCN) within SONATA BIS 12 (project no. 2022/46/E/ST8/00284 to M.C.), and Ministero dell'Istruzione, dell'Università e della Ricerca (PRIN funding scheme no. 201742SBXA_004 and 2022F37JRF to C.G.). We would like to thank Dr. Mario Bragaglia and Dr. Lorenzo Paleari, Materials Science and Technology group, Department of Enterprise Engineering, University of Rome Tor Vergata, for the precious help in performing mechanical analysis.

Conflicts of Interest

The authors declare no conflicts of interest.

Data Availability Statement

The mass spectrometry proteomics data are available at the ProteomeXchange Consortium via the PRIDE partner repository with the dataset identifier PXD043605.

References

1. H. Kim, T. Osaki, R. D. Kamm, and H. H. Asada, "Multiscale Engineered Human Skeletal Muscles With Perfusable Vasculature and Microvascular Network Recapitulating the Fluid Compartments," *Biofabrication* 15 (2022): 15005.

2. M. Costantini, S. Testa, E. Fornetti, et al., "Biofabricating Murine and Human Myo-Substitutes for Rapid Volumetric Muscle Loss Restoration," *EMBO Molecular Medicine* 13 (2021): e12778.

3. E. Fornetti, F. De Paolis, C. Fuoco, et al., "A Novel Extrusion-Based 3D Bioprinting System for Skeletal Muscle Tissue Engineering," *Biofabrication* 15 (2023): 25009.

4. M. Volpi, A. Paradiso, M. Costantini, and W. Święszkowski, "Hydrogel-Based Fiber Biofabrication Techniques for Skeletal Muscle Tissue Engineering," *ACS Biomaterials Science & Engineering* 8 (2022): 379–405.

5. E. Fornetti, S. Testa, F. De Paolis, et al., "Dystrophic Muscle Affects Motoneuron Axon Outgrowth and NMJ Assembly," *Advanced Materials Technology* 7 (2022): 2101216.

6. Y. Leng, X. Li, F. Zheng, et al., "Advances in In Vitro Models of Neuromuscular Junction: Focusing on Organ-on-a-Chip, Organoids, and Biohybrid Robotics," *Advanced Materials* 35 (2023): 2211059.

7. M. R. Ladd, S. J. Lee, J. D. Stitzel, A. Atala, and J. J. Yoo, "Co-Electrospun Dual Scaffolding System With Potential for Muscle–Tendon Junction Tissue Engineering," *Biomaterials* 32 (2011): 1549–1559.

8. M. A. Bakooshli, E. S. Lippmann, B. Mulcahy, et al., "A Three-Dimensional Culture Model of Innervated Human Skeletal Muscle Enables Studies of the Adult Neuromuscular Junction and Disease Modeling," *BioRxiv* (2018): 275545.

9. D. Jeong, J. W. Seo, H.-G. Lee, W. K. Jung, Y. H. Park, and H. Bae, "Efficient Myogenic/Adipogenic Transdifferentiation of Bovine Fibroblasts

in a 3D Bioprinting System for Steak-Type Cultured Meat Production," *Advancement of Science* 9 (2022): 2202877.

10. A. Shahin-Shamsabadi and P. R. Selvaganapathy, "Engineering Murine Adipocytes and Skeletal Muscle Cells in Meat-Like Constructs Using Self-Assembled Layer-by-Layer Biofabrication: A Platform for Development of Cultivated Meat," *Cells Tissues Organs* 211 (2022): 304–312.

11. A. Dellavalle, M. Sampaolesi, R. Tonlorenzi, et al., "Pericytes of Human Skeletal Muscle Are Myogenic Precursors Distinct From Satellite Cells," *Nature Cell Biology* 9 (2007): 255–267.

12. A. Dellavalle, G. Maroli, D. Covarello, et al., "Pericytes Resident in Postnatal Skeletal Muscle Differentiate Into Muscle Fibres and Generate Satellite Cells," *Nature Communications* 2 (2011): 499.

13. B. Sacchetti, A. Funari, S. Michienzi, et al., "Self-Renewing Osteoprogenitors in Bone Marrow Sinusoids Can Organize a Hematopoietic Microenvironment," *Cell* 131 (2007): 324–336.

14. B. Sacchetti, A. Funari, C. Remoli, et al., "No Identical 'Mesenchymal Stem Cells' at Different Times and Sites: Human Committed Progenitors of Distinct Origin and Differentiation Potential Are Incorporated as Adventitial Cells in Microvessels," *Stem Cell Reports* 6 (2016): 897–913.

15. S. Testa, C. S. Riera, E. Fornetti, et al., "Skeletal Muscle-Derived Human Mesenchymal Stem Cells: Influence of Different Culture Conditions on Proliferative and Myogenic Capabilities," *Frontiers in Physiology* 11 (2020): 553198.

16. G. Cossu, S. C. Previtali, S. Napolitano, et al., "Intra-Arterial Transplantation of HLA-Matched Donor Mesoangioblasts in Duchenne Muscular Dystrophy," *EMBO Molecular Medicine* 7 (2015): 1513–1528.

17. M. Costantini, S. Testa, P. Mozetic, et al., "Microfluidic-Enhanced 3D Bioprinting of Aligned Myoblast-Laden Hydrogels Leads to Functionally Organized Myofibers In Vitro and In Vivo," *Biomaterials* 131 (2017): 98–110.

18. C. Fuoco, R. Rizzi, A. Biondo, et al., "In Vivo Generation of a Mature and Functional Artificial Skeletal Muscle," *EMBO Molecular Medicine* 7 (2015): 411–422.

19. M. Volpi, A. Paradiso, E. Walejewska, C. Gargioli, M. Costantini, and W. Swieszkowski, "Automated Microfluidics-Assisted Hydrogel-Based Wet-Spinning for the Biofabrication of Biomimetic Engineered Myotendinous Junction," *Advanced Healthcare Materials* (2024): 2402075.

20. N. Celikkin, D. Presutti, F. Maiullari, et al., "Combining Rotary Wet-Spinning Biofabrication and Electro-Mechanical Stimulation for the In Vitro Production of Functional Myo-Substitutes," *Biofabrication* 15 (2023): 45012.

21. C. Fuoco, E. Sangalli, R. Vono, et al., "3D Hydrogel Environment Rejuvenates Aged Pericytes for Skeletal Muscle Tissue Engineering," *Frontiers in Physiology* 5 (2014): 203.

22. C. Fuoco, M. L. Salvatori, A. Biondo, et al., "Injectable Polyethylene Glycol-Fibrinogen Hydrogel Adjuvant Improves Survival and Differentiation of Transplanted Mesoangioblasts in Acute and Chronic Skeletal-Muscle Degeneration," *Skeletal Muscle* 2 (2012): 1–14.

23. P. Zhu, Y. Zhou, F. Wu, et al., "Selective Expansion of Skeletal Muscle Stem Cells From Bulk Muscle Cells in Soft Three-Dimensional Fibrin Gel," *Stem Cells Translational Medicine* 6 (2017): 1412–1423.

24. C. Mueller, M. Trujillo-Miranda, M. Maier, D. E. Heath, A. J. O'connor, and S. Salehi, "Effects of External Stimulators on Engineered Skeletal Muscle Tissue Maturation," *Advanced Materials Interfaces* 8 (2021): 2001167.

25. A. Reggio, M. Rosina, N. Krahmer, et al., "Metabolic Reprogramming of Fibro/Adipogenic Progenitors Facilitates Muscle Regeneration," *Life Science Alliance* 3 (2020): e202000646.

26. A. Reggio, F. De Paolis, S. Bousselmi, et al., "Development of a Platform of 3D Adipogenesis to Model, at Higher Scale, the Impact of LY2090314 Compound on Fibro/Adipogenic Progenitor Adipogenic Drift," *Disease Models & Mechanisms* 16 (2023): dmm049915.

27. S. Tyanova, T. Temu, P. Sinitcyn, et al., "The Perseus Computational Platform for Comprehensive Analysis of (Prote)omics Data," *Nature Methods* 13 (2016): 731–740.

28. C. M. Dorman and S. E. Johnson, "Activated Raf Inhibits Avian Myogenesis Through a MAPK-Dependent Mechanism," *Oncogene* 18 (1999): 5167–5176.

29. L. L. Tortorella, D. J. Milasincic, and P. F. Pilch, "Critical Proliferation-Independent Window for Basic Fibroblast Growth Factor Repression of Myogenesis via the p42/p44 MAPK Signaling Pathway," *Journal of Biological Chemistry* 276 (2001): 13709–13717.

30. N. J. Turner and S. F. Badylak, "Regeneration of Skeletal Muscle," *Cell and Tissue Research* 347 (2012): 759–774.

31. S. E. Anderson, W. M. Han, V. Srinivasa, et al., "Determination of a Critical Size Threshold for Volumetric Muscle Loss in the Mouse Quadriceps," *Tissue Engineering Part C, Methods* 25 (2019): 59–70.

32. N. Celikkin, D. Presutti, F. Maiullari, et al., "Tackling Current Biomedical Challenges With Frontier Biofabrication and Organ-on-a-Chip Technologies," *Frontiers in Bioengineering and Biotechnology* 9 (2021): 732130.

33. D. Dikovsky, H. Bianco-Peled, and D. Seliktar, "The Effect of Structural Alterations of PEG-Fibrinogen Hydrogel Scaffolds on 3-D Cellular Morphology and Cellular Migration," *Biomaterials* 27 (2006): 1496–1506.

34. M. Gonen-Wadmany, R. Goldshmid, and D. Seliktar, "Biological and Mechanical Implications of PEGylating Proteins Into Hydrogel Biomaterials," *Biomaterials* 32 (2011): 6025–6033.

35. H. Simaan-Yameen, O. Bar-Am, G. Saar, and D. Seliktar, "Methacrylated Fibrinogen Hydrogels for 3D Cell Culture and Delivery," *Acta Biomaterialia* 164 (2023): 94–110.

36. A. Reggio, V. Buonomo, R. Berkane, et al., "Role of FAM134 Paralogues in Endoplasmic Reticulum Remodeling, ER-Phagy, and Collagen Quality Control," *EMBO Reports* 22 (2021): e52289.

37. M. Marinkovic, C. Fuoco, F. Sacco, et al., "Fibro-Adipogenic Progenitors of Dystrophic Mice Are Insensitive to NOTCH Regulation of Adipogenesis," *Life Science Alliance* 2 (2019): e201900437.

38. L. Perfetto, L. Briganti, A. Calderone, et al., "SIGNOR: A Database of Causal Relationships Between Biological Entities," *Nucleic Acids Research* 44 (2016): D548–D554.

39. A. Palma, A. Cerquone Perpetuini, F. Ferrentino, et al., "Myo-REG: A Portal for Signaling Interactions in Muscle Regeneration," *Frontiers in Physiology* 10 (2019): 1216.

Supporting Information

Additional supporting information can be found online in the Supporting Information section.